Tip-Shroud Cutbacks in a Low-Pressure Gas Turbine Stage

Patrick S. Rebholz* and Reza S. Abhari†
Swiss Federal Institute of Technology, 8092 Zurich, Switzerland
Anestis I. Kalfas‡
Aristotle University of Thessaloniki, 541 24 Thessaloniki, Greece
and
Carsten Zscherp§
MTU Aero Engines AG, 80995 Munich, Germany

This paper presents an experimental and computational study of tip-shroud modifications in a low-pressure gas turbine. Partial shrouds are a viable option to reduce the static stresses in high-speed stages compared to full shrouds while still benefiting from superior aerodynamic efficiency compared to unshrouded blades. Three different tip-shroud platform cutbacks have been tested experimentally in a low-aspect-ratio 1.5-stage low-pressure axial turbine and are compared to a full-shroud baseline. A detailed analysis of the fluid dynamics is carried out to provide a starting point for shroud optimizations. The leading- and trailing-edge platforms are cut back separately to isolate the effect of each modification. The final rotor then features a combined partial shroud on both leading and trailing edge, with the same material reduction as the shroud leading-edge cutback. The time-resolved flowfield and pressure measurements are accompanied by three-dimensional, unsteady Reynolds-averaged Navier–Stokes simulations, which provide insight into the over-tip leakage flows and their interaction with the main flow both at cavity inlet and outlet. The aerodynamic losses with the trailing-edge cutback are reduced compared to the baseline, but the resulting underturning from the interaction with the shroud exit cavity makes it inferior in terms of efficiency compared to the leading-edge cutback. The isolated shroud leading-edge cutback shows the best tradeoff between stress reduction and aerodynamic efficiency penalty (0.7%).

Nomenclature

C_{ax}	=	axial chord
IR	=	injection rate
$\dot{m}$	=	mass flow
N	=	rotational speed
p	=	pressure
Re	=	Reynolds number
T	=	temperature
v	=	velocity
$\bar{x}$	=	x normalized by value of x at turbine inlet
γ	=	specific heat ratio
Δs	=	entropy change
η	=	efficiency
Π	=	pressure ratio
Ω	=	vorticity

Subscripts

in	=	turbine inlet
max	=	maximum
r	=	radial
rel	=	rotor relative
s	=	streamwise
stage	=	single stage
tt	=	total-to-total

0	=	stagnation flow quantity
1.5	=	across one-and-one-half stages

I. Introduction

TURBOMACHINES are sophisticated and multidisciplinary machines. Especially for aeroengines, the interaction between aerodynamics, thermal management, and mechanics leads to a tradeoff between different design parameters. In high-pressure turbines, shrouds are favorable aerodynamically for the low-aspect-ratio blading but are not always used due to the high effort and high manufacturing cost that has to be spent on the cooling design in a high-temperature environment. All modern engines for wide-body aircrafts with low-speed low-pressure turbines feature a shroud on all low-pressure turbine stages. There are two main reasons for shrouded low-pressure turbine blades: the superior aerodynamic efficiency, and the reduction of blade flutter for high-aspect-ratio blades [1]. Stress and weight reduction and aerodynamics often have opposed optimization goals. For current engine concepts, the weighting of different design parameters is shifted toward mechanical design [2,3]. Because the centrifugal forces on the blades are proportional to the square of the rotational speed, the mass concentration at the tip of the blade represented by a shroud becomes more critical for high-speed low-pressure turbines. The aerodynamic superiority is sacrificed for a reduction of mean stress in this case. Therefore, representatives of this engine family do not feature a shroud on the low-pressure turbine blades. The reduction of part count for the same power output significantly increases the loading of low-pressure turbine blades and needs to be considered in the high cycle fatigue assessment.

For low-aspect-ratio blades like those in high-pressure turbines, roughly up to 30% of the generated aerodynamic loss could be associated to leakage flows [4]. In terms of efficiency improvements, a shroud has the highest impact here, which is also why the most research has been done on high-pressure turbines. Unshrouded low-pressure turbine blading has been recently investigated by Selic et al. [5], but they focused on the effect on the exit guide vane rather than the losses associated to the turbine itself. The challenge for high pressure (HP) turbines, however, is to not expend too much bypass air from the compressor on cooling the shroud. Harvey [6] presents the

most comprehensive overview on blade-tip design. It is shown qualitatively that unshrouded turbines are, in terms of losses, much more sensitive to tip clearance than shrouded turbines. With respect to hypothetical zero tip gap, unshrouded HP turbines create twice as much loss as a two-finned shroud configuration. To avoid aerothermal problems with an high pressure turbine (HPT) shroud, various other solutions have been investigated to reduce the tip leakage flow of unshrouded turbines. With different tip squealer geometries, the tip gap is reduced. Reducing the contact area between the casing and blade also reduces the risk of damage by rubbing. Kaiser and Bindon [7], Camci et al. [4], Mischo et al. [8], and others have shown beneficial impact on the loss generation using various squealer geometries. Adding winglets onto the blade tip is a step further toward a shrouded turbine. In combination with grooves and other features, a vast set of winglet geometries has been investigated and proven to enhance aerodynamic performance by Harvey and Ramsden [9], Dey and Camci [10], Zhou et al. [11], and others. However, both squealers and winglets do not provide additional stiffness to the blade row and are therefore more viable for high-pressure turbines.

For full shrouds, the aerodynamic losses generated by the over-tip leakage and the mixing losses created by the interaction of leakage fluid and main flow have been studied by various authors. Denton analytically derived the losses for shrouded turbines with a single sealing fin [12]. Wallis et al. [13] defined four main loss generation mechanisms for leakage flows in shrouded axial turbines. The bypassing of the rotor, the mixing in the shroud cavity, the mixing with the main flow, and the flow angle deviation on the downstream stage are the main contributors to entropy generation. They used radial fins on the shroud to reduce the underturning of leakage, which resulted in a reduction of efficiency. Contrary to the fins in the rotating system, the installation of turning vanes in the shroud exit cavity applied by Rosic and Denton [14] resulted in an increased efficiency of 0.4% due to an improvement of the flowfield in the downstream blade row. Anker et al. [15] numerically studied the interaction of shroud leakage fluid with the main flow for different clearance gaps. They found a significant impact on the formation of secondary flows in both the rotor and the downstream stator. Pfau et al. [16] studied the influence of open cavities and proposed to introduce nonaxisymmetric shrouds and cavities to recover work from the leakage fluid and improve the interaction with the secondary flows. Barmpalias et al. [17] systematically varied the geometry of the shroud inlet cavity of a steam turbine rotor. The toroidal vortex structures present in the cavity are found to play a major role in the interaction between the main flow and the cavity fluid. With a careful design of the cavity, the vortices can facilitate the reentry of cavity fluid into the main flow. The investigations of Giboni et al. [18], Rosic et al. [19], Barmpalias et al. [20], and others emphasize that the cavity flows and the interaction with the main flow is highly unsteady and three-dimensional. The cavity flowfield and the impact on the overall performance are sensitive to the geometry of the cavity and the rotor shroud. The effect of shroud leakage flows is investigated based on a numerical analysis specifically for a low-pressure turbine configuration by Gier et al. [21]. In a similar loss distinction as proposed by Wallis et al. [13], the main losses (about 50%) were attributed to mixing, whereas bypass losses and losses associated to steps in the flow path were found to make up for 20% of the overall cavity losses.

Most of the studies on full shrouds mentioned have been performed for power-generation turbines. Shrouds can be more easily accommodated here because the additional weight of stronger blades does not represent such a major drawback as for propulsion systems. Studies on partial shrouds covering the full passage are scarce in open literature. Nirmalan and Bailey [22] investigated three different shroud geometries in a cascade with a single fin. For a small tip gap, the total pressure loss of the full shroud was found to be 1% less compared to a medium scallop shroud and 2% less compared to a deep scallop shroud. For increased tip clearances, the sensitivity of performance to the shroud geometry is reduced. Porreca et al. [23] found that the opening of the rotor blade throat by removing the shroud trailing-edge platform leads to a considerable performance reduction. The tip-passage vortex strength is enhanced by the partial

shroud and convected through the downstream rows. The comparison between the full shroud and the partial shroud appears difficult because the authors found that small changes in the cavity geometry have a significant effect on the main flow. The optimized design with a covered blade throat shows a total-to-total efficiency improvement of 0.6% [24]. However, the performance of the fully shrouded rotor remains superior by 0.5%. Except for the publications by Porreca et al. [23], Feldman et al. [25] (cascade), and Nirmalan and Bailey [22] (cascade), no data on partial shrouds in turbines are available.

Partial shrouds would be a viable option to reduce mean blade stress compared to a full shroud while still benefitting from the superior aerodynamics and the robustness against flutter compared to unshrouded blades. There are little data available on partial shrouds in low-pressure turbines in open literature. The experimental and numerical investigation carried out in this paper isolates the effect of leading- and trailing-edge platform effects and provides detailed information on the flow physics and associated losses. This information indicates the limits of stress reduction early in the design phase and can help to decide whether a shrouded configuration is viable at all.

II.   Experimental Method

The experimental investigation was performed in the "LISA" research turbine at the Laboratory for Energy Conversion (LEC) at the Swiss Federal Institute of Technology in Zurich (ETH Zurich). A detailed description is presented by Behr et al. [26].

A.   Research Turbine Facility

The research turbine shown in Fig. 1 is a quasi-closed-loop facility. The inlet pressure is generated by a radial compressor. The inlet total temperature $T_{0,in}$ is controlled to ± 0.2 K with a two-stage water-to-air heat exchanger, and the mass flow is measured with a calibrated Venturi nozzle. A homogeneous flowfield is created by a 3 m flow conditioning stretch before the flow enters the test section. The acceleration in the contraction helps reducing flow nonuniformities. The flow undergoes a subatmospheric expansion through the 1.5 stages. After pressure is recovered to atmospheric level, the air loop is open to atmosphere downstream of the turbine. The recovery of the static pressure with a tandem deswirl vane row is required due to the compressor's limited compression of $\Pi_{c,max} = 1.4$. The rotational speed of the turbine of 2700 rpm is controlled by a dc generator to an accuracy of ± 0.5 rpm. The turbine torque is measured by a
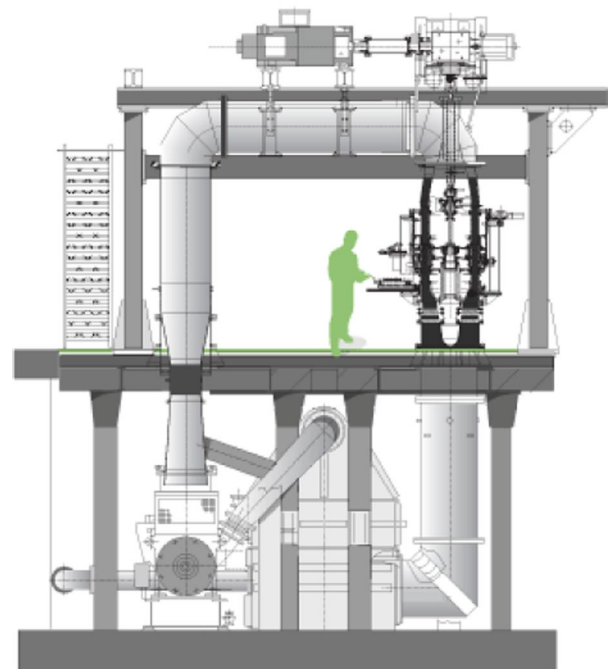
Fig. 1   Overview of the LISA test facility at the LEC at ETH Zurich.

torquemeter. The first vane row exit flow is compressible with a Mach number of 0.52.

B. Operating Conditions

The operating conditions are summarized in Table 1. The total-to-static pressure ratio across the 1.5-stage test section is kept constant for all measurements at $\Pi_{1.5} = 1.65$. The inlet total temperature is also kept constant at $T_{0,in} = 328$ K. A constant amount of purge flow of 0.8% of the main mass flow (typically 11.8 kg/s) is injected at the hub between the first vane and the rotor. The injection system is described more in detail by Schuepbach et al. [27]. Because of the opening to atmosphere at the exit of the turbine, all thermodynamic flow quantities are normalized by the inlet stagnation conditions. This procedure allows for an accurate comparison between different measurement days.

C. Shroud Cutback Designs

This low-pressure turbine configuration is based on the design used by Jenny et al. [28]. For the partial shrouds, material has been removed from the leading- and trailing-edge platform based on the results from Porreca et al. [24]. The end walls of the first vane row are profiled at the hub and tip, whereas the second vane has cylindrical end walls. The hub end wall profiling as well as the blade geometry of the rotor are identical to previous experiments and are the same for all cutback designs. For the baseline, the shroud features a cylindrical end wall to allow for modifications. To provide more space for the shroud leading-edge modification, the first sealing fin is placed 5% of the axial cavity length (7% of the rotor tip axial chord) away from the cavity inlet, increasing the inlet cavity volume by 17%.

Three shroud cutback designs have been tested in addition to the full shroud baseline. Figure 2 illustrates the three different shroud platform cutback shapes under investigation. The intention of the four tested shroud designs is to identify the cutback location for the best tradeoff between material removal and aerodynamic loss generation. Figure 2a shows the geometry of the shroud leading-edge platform cutback, referred to as leading-edge (LE) cutback. For this design, the maximum amount of material (11.6% of full shroud) has been removed upstream of the first shroud sealing fin. Only a semicircular platform is left over the leading edge of the blade, in order not to alter the fillet connecting the blade to the shroud. The center of the arc has been chosen such that parts of the pressure side are still shielded from the shroud cavity. A separate rotor featuring a partial shroud at the trailing edge, referred to as trailing-edge (TE) cutback, is designed based on the findings in Porreca et al. [23]. As shown in Fig. 2b, the shroud trailing-edge platform is cut back to the maximum extent while leaving the throat area of the turbine and the fillet unaltered. The opening of the shroud exit cavity to the main flow starts 78% of rotor axial chord earlier in the streamwise direction than for the unmodified platform. The overall material reduction equals 5.3% for this design (i.e., less than half compared to the LE cutback). Because it is expected to have better performance with the TE cutback, material is also removed from the leading-edge platform of the TE cutback rotor. The shape of the combined cutback at the leading-edge platform is offset from the LE cutback by 1.2% of the
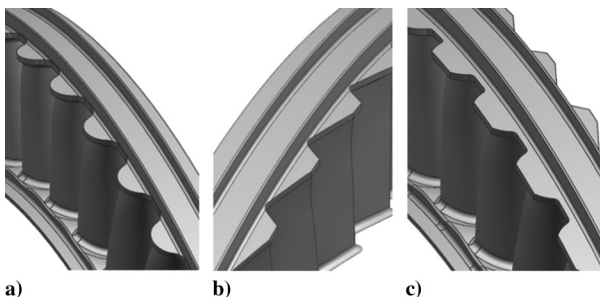
rotor axial chord to obtain the identical mass reduction as for the LE cutback (total of 11.6% material removal).

D. Measurement Planes

The traverse data presented in this paper are acquired downstream of the rotor and downstream of the second stator, as shown in Fig. 3. The spatial resolution of the measurement grid covered 42 radial and 41 equally spaced circumferential points covering one stator pitch. The radial resolution is refined close to the end walls.

Pneumatic tappings and pressure transducers are installed on the outer tip-shroud cavity wall. In the inlet cavity (1) and the exit cavity (3) in Fig. 4, the axial resolution of the tappings is 3% of the axial cavity dimension and 6% for the transducers, respectively.

E. Measurement Technology

The performance of the different cutback configurations is derived from the steady flowfield, which has been measured with a cobra-shaped pneumatic five-hole probe (5 HP) with a head diameter of 0.9 mm. The unsteady flowfield is captured with a two-sensor fast-response aerodynamic probe (FRAP) and a fast-response entropy probe (FENT). Both FRAP and FENT have been developed at ETH Zurich (Kupferschmied et al. [29], Pfau et al. [30], and Mansour et al. [31]) and have a head diameter of 1.8 mm. The probes resolve flowfield oscillations with frequencies up to 48 kHz for the FRAP and 40 kHz for the FENT. For the FRAP, the measurement of temperature is limited to 10 Hz. Therefore, the simultaneous measurements of pressure and temperature are done with the FENT probe to derive the change in static entropy. The FRAP is operated in a virtual four-sensor mode, allowing the measurement of the three-dimensional and time-resolved flowfield. Table 2 shows the relative uncertainty of the 5 HP and FRAP relative to the calibration range of ±30 deg for the yaw angle and ±20 deg for the pitch angle and as a percentage of the dynamic head for the total and static pressure. The relative uncertainties of the FENT probe are summarized in Table 3. The data are acquired at a sampling rate of 200 kHz over a period of 2 s. Three consecutive rotor blade passings are considered in the postprocessing and phase-lock averaged 85 times.

The uncertainty of the pneumatic tapping measurements of the static wall pressure on the outer shroud cavity wall is estimated to be 0.02% of the inlet total pressure. The expanded uncertainty for the time-resolved wall pressure measurements has been estimated to be 0.1% of the inlet total pressure by Behr [32]. The unsteady wall pressure is recorded with a sampling rate of 100 kHz for 3 s and phase-lock averaged in a similar fashion as the FRAP data.
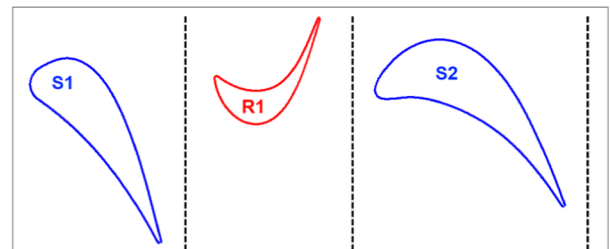
Fig. 3 Sketch of the measurement plane locations upstream and downstream of the rotor and downstream of the second stator.
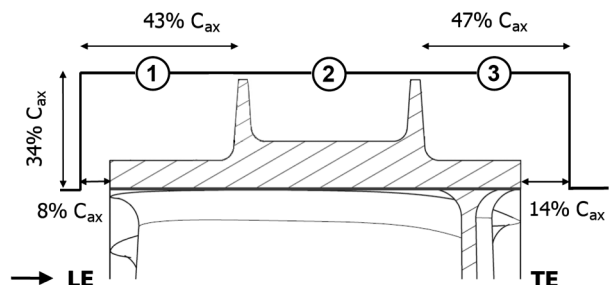
Fig. 4 Sketch of inlet (1), intermediate (2), and exit cavity (3). Dimensions are normalized by the rotor tip axial chord. The tip gap is 0.7 mm.

a) b) c)

Fig. 2 The three tested shroud cutback geometries: a) leading-edge cutback, b) trailing-edge cutback, and c) combined cutback.

Table 1 Operating conditions and geometrical characteristics

Parameter	Value
$\Pi_{1.5}$	$1.65 \pm 0.4\%$
$T_{0,\text{in}}$	328 ± 0.3 K
$\dot{m}\sqrt{T_{0,\text{in}}}/p_{0,\text{in}}$	152 ± 0.2 kg $\cdot$ K$^{0.5}$ $\cdot$ s^{-1} $\cdot$ bar^{-1}
$N/\sqrt{T_{0,\text{in}}}$	2.48 ± 0.05 rps $\cdot$ K$^{-0.5}$
Mach number ($S1$ ex/$R1$ ex/$S2$ ex)	0.52/0.28/0.48
Reynolds number ($S1/R/S2$)	$7.1/3.8/5.1 \times 10^5$

Table 2 Relative uncertainty of the 5 HP and the FRAP

Probe	Yaw, %	Pitch, %	p_0, %	p, %
5 HP	0.5	0.8	0.6	1.0
FRAP	0.8	2.3	1.0	1.2

Table 3 Relative uncertainty of the FENT [33]

p_{ref}	T_{ref}	P_0	T_0	Δs
0.016%	0.12%	0.1%	2.5%	2.51%

III. Computational Method

A. Grid and Boundary Conditions

The computational domain covers two stator blade pitches of the 1.5-stage configuration (i.e., a 2–3–2 blade count is meshed). The mesh of the time-resolved simulations is structured and consists of approximately 40 million nodes. It is refined in the areas of interaction between the main flow and the cavities as well as in the high shear regions, like the blade wake. The boundary conditions in the circumferential direction are set to be periodic. The rim cavity between the first stator and rotor is also modeled to obtain the correct reaction and mass flow distribution. The boundary conditions at the inlet and the outlet of the turbine are according to performance measurements. At the domain inlet, the total pressure and total temperature are specified accordingly, whereas at the first stator hub cavity and at the outlet of the second stator, constant mass flows are applied.

B. Solver

All presented calculations were carried out with ANSYS CFX Version 13. A steady-state run was performed to provide an initial condition for the time-resolved simulations. The time step was set to 160 steps per period, which is equivalent to a 0.125 deg rotation of the rotating domain per time step. The resulting mean Courant-Friedrichs-Lewy (CFL) number is less than 7. The shear-stress transport turbulence model without turbulence transition modeling was applied. The maximum residuals were found to be in the order of 10^{-3}, whereas the mass imbalance is in the order of 10^{-6}. The
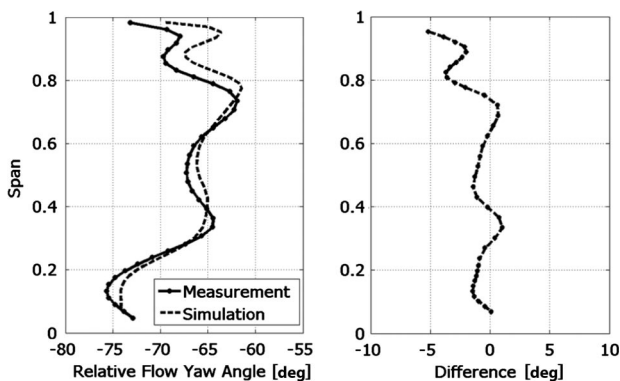
correlation coefficient of static entropy monitoring points at rotor exit was used to assess the periodic convergence of the unsteady simulations. Periodic convergence was assumed to be reached when the correlation coefficient was 99% or higher.

C. Validation

In the following section, the computational results of only the LE cutback case are compared to measurements for the sake of clarity. The LE cutback represents the most severe change in geometry compared to previously validated models as in [28]. The presented results are comparable for the other simulated cases, baseline and TE cutback.

Three rotor blade passings of the time-resolved simulation are considered for the comparison with experimental data. The computational fluid dynamics (CFD) results are processed in the same way as the time-resolved measurements.

Figure 5 shows the comparison of the time- and circumferentially mass-averaged relative flow yaw angle at rotor exit between computation and experiment for the LE cutback case. The relative yaw angle at rotor exit agrees well between simulation and experiment. The dominant flow features are well represented by the simulation, as shown in Fig. 5. The absolute deviation is within ± 2 deg below 75% span. The radial position and amplitude of the overturning–underturning structure close to the tip end wall deviate more than the main flow. The maximum difference found here is -6 deg for the relative flow yaw angle.

Figure 6 shows the spatial distribution of the time-averaged normalized total pressure at the rotor exit in the rotating frame of reference. The loss regions associated to the rotor wake, the rotor hub passage vortex, and the interaction zone with the shroud exit cavity close to the tip end wall agree well between experiment (Fig. 6a) and computation (Fig. 6b) in terms of shape, size, and position. However, the computations tend to slightly overpredict the total pressure loss in the wake (0.5%) and the hub passage vortex (1%). The total pressure level in the main flow and the interaction zone with the shroud exit cavity agree well (less than 0.5% difference).

For the LE cutback, the static wall pressure in the shroud inlet cavity agrees well with the measurements, as shown in Fig. 7. The predicted static pressure drop across the first sealing fin is overpredicted by 1%. In the intermediate cavity, the average pressure level drops in the simulations and is 2% less than in the measurements. This leads to a lower static pressure drop across the second fin in the simulations. The general pressure trend in the exit cavity is captured by the CFD, but the mean level is overpredicted by 1%. The overall axial pressure ratio across the shroud is predicted to be lower than the measurements (i.e., the estimated over-tip leakage mass flow will be less than the real leakage flow).

In terms of performance, CFD tends to underpredict the absolute level of integrated efficiency at the rotor exit measurement plane as defined in Eq. (1) with this setup for the fully shrouded baseline (0.39%) and the TE cutback (0.74%). For the LE cutback, the performance is overpredicted by 0.3%.

Fig. 5 Comparison between calculation and measurement of the relative flow yaw angle at rotor exit for the LE cutback case.
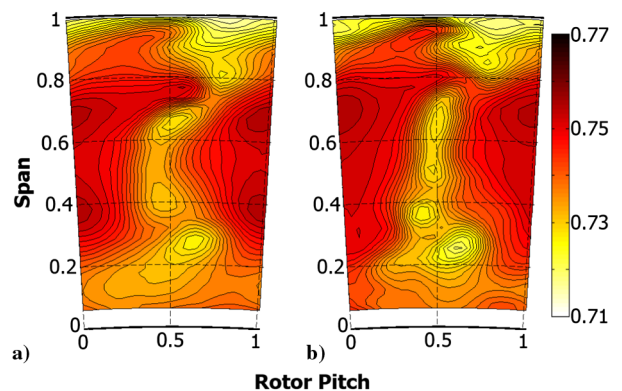
Fig. 6 Single rotor pitch of time-averaged, normalized total pressure at rotor exit in the rotating frame for the LE cutback: a) experiment and b) computation.
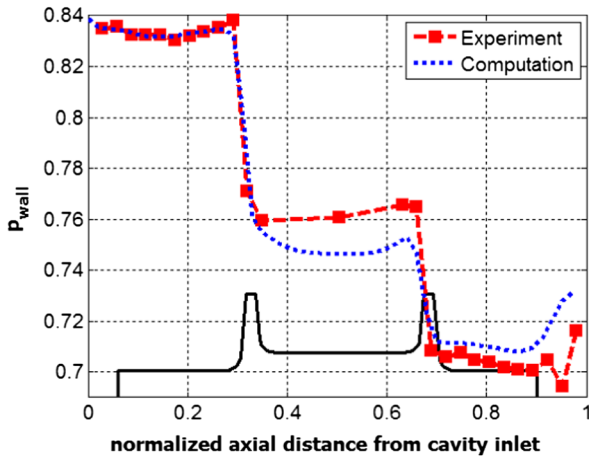
Fig. 7   Comparison of the experimentally and numerically determined normalized static wall pressure in the rotor tip-shroud cavity for the LE cutback.

IV.   Results and Discussion

The aerodynamic performance of the shroud cutbacks is compared to the full shroud baseline in Fig. 8 in terms of total-to-total stage efficiency as defined in Eq. (1):

$$\eta_{tt} = \frac{\omega M / \dot{m} c_p T_{0,in}}{1 - (1 - IR)(p_{0,R1\,ex}/p_{0,in})^{\gamma/\gamma-1} - IR(p_{0,R1\,ex}/p_{0,cavity})^{\gamma/\gamma-1}}$$

$$(1)$$

All shroud cutbacks result in a reduction of efficiency. The reduction for the LE and TE cutback is 0.7% relative to the baseline. Their difference is within the measurement uncertainty. For the combined cutback, the losses add up to 1.1% reduction of efficiency. In the case of the LE cutback, the deterioration of performance is related not only to aerodynamics directly but also to a reduction of capacity of approximately 0.3%.

For the geometries featuring a TE cutback, the capacity is unaltered, but the flow is underturned in the rotor by, on average, 2 deg in the main flow region around midspan. The associated deficit in change of angular momentum correlates well with the detected torque reduction and the rise in total pressure at the rotor exit. The causes of these observations are discussed in detail in the following sections.

Except for the reduction of the mass flow for the LE cutback, the rotor inlet flowfield has not been measurably affected on the measurement plane upstream of the rotor.

A.   Rotor Exit Flowfield

The most significant impact of the shroud cutbacks is well summarized by the pitchwise mass-averaged relative flow yaw angle at rotor exit as shown in Fig. 9. From the hub to 35% span, the overturning–underturning characteristic caused by the rotor hub passage vortex is clearly visible for the baseline. This region of the
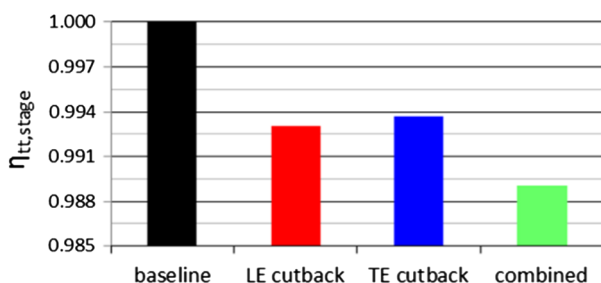
Fig. 8   Normalized single-stage total-to-total efficiency of all test configurations.
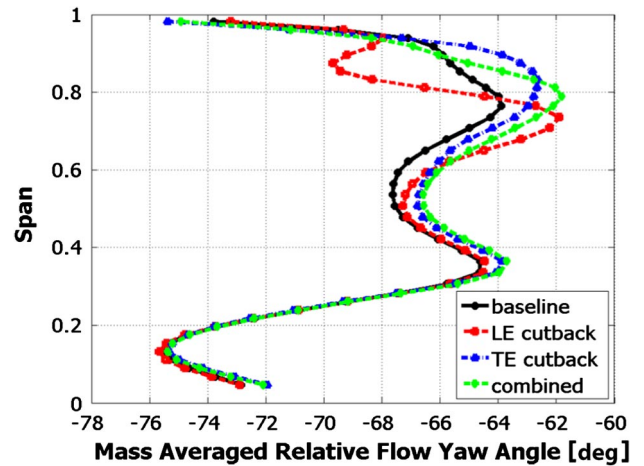
Fig. 9   Experimentally measured pitchwise mass-averaged relative flow yaw angle at rotor exit.

flow remains unaffected by the cutback at the tip shroud. The tip-passage vortex extends from 75 to 95% span for the baseline. Similar to the baseline, the center of the tip-passage vortex region is located at 80% span. However, the underturning region reaches 5% farther toward midspan. Compared to the baseline, the incidence on the downstream vane is therefore −5 deg at 70% span and +8 deg at 85% span when compared to the baseline. This is both absolute and in terms of variation the highest value for all tested cutbacks and indicates a significant increase in the tip-passage vortex strength.

For both TE and combined cutback, the influence of the shroud modification is already visible at 35% span. In the main flow up to 70% span, the flow is underturned by, on average, −2 deg. The tip-passage vortex is weakened and disappears temporarily in the time-resolved data. Because of the intrusion into the shroud exit cavity, the flow will have an incidence of +8 deg at 98% span on the downstream vane.

The combined cutback shows trends observed for both the LE cutback and the TE cutback. Because the rotor exit measurement plane is closer to the shroud trailing edge and the amount of material removed from the leading-edge platform is less than in the LE cutback case, the effects of the shroud trailing-edge modification are dominant (i.e., the underturning in the main flow is the same as for the TE cutback). An underturning–overturning feature typical for the tip-passage vortex with its center being at 85% span is then superimposed onto the TE cutback characteristic by the shroud leading-edge modification.

Figure 10 shows the time-averaged streamwise vorticity in the rotor relative frame at the rotor exit for the baseline and the two isolated cutbacks from 60% span to the tip. Similar to what is described in Fig. 9, the flowfield for the TE cutback (Fig. 10c) and the combined cutback (Fig. 10d) are almost identical due to the dominant impact of the shroud trailing-edge modification. The following statements on the TE cutback can therefore be translated to the combined cutback.

Region 1 indicates the roll-up of the wake close to the tip. These regions are associated with high positive streamwise vorticity from 60 to 95% span in all test cases and mark the position of the rotor wake. The position slightly varies in the pitchwise direction due to different rotor mounting positions relative to the trigger system.

For the baseline (Fig. 10a) and the LE cutback (Fig. 10b), a concentrated region of negative streamwise vorticity associated to the tip-passage vortex is found at 80% span on the suction side of the rotor wake. The integral comparison of two regions bounded by an isoline of streamwise vorticity (−2500 Hz) shows that not only the size but also the strength of the passage vortex is increased for the LE cutback. The vortex area grows by a factor of 4.5, covering now 8% of the annulus area. The circulation is increased by a factor of 6.5, indicating a significant intensification of the tip-passage vortex. This is also indicated by the enhanced counterclockwise inclination of the tip part of the rotor wake (3) caused by the interaction between the
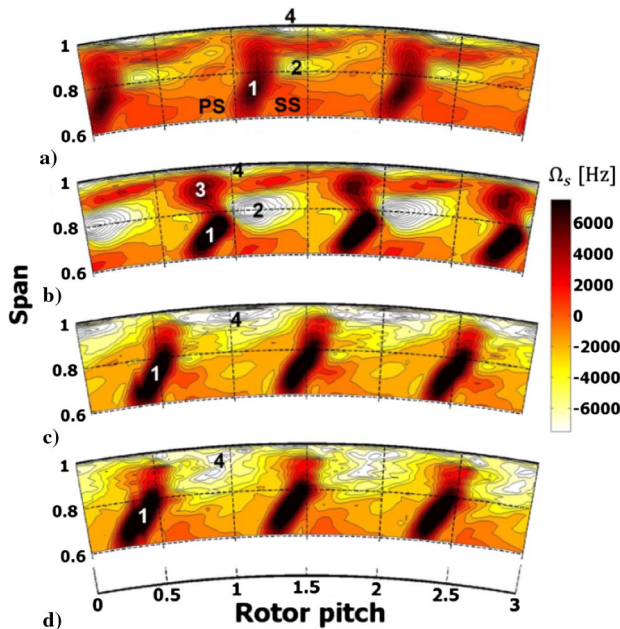
Fig. 10 Time-averaged streamwise vorticity at rotor exit in the rotor relative frame: a) baseline, b) LE cutback, c) TE cutback, and d) combined cutback.

Fig. 11 Time-averaged static entropy change at rotor exit in the rotor relative frame: a) baseline, b) LE cutback, c) TE cutback, and d) combined cutback.

sheetlike radial vorticity in the wake and the tip-passage vortex. The tip-passage vortex carries high-turbulence, low-momentum fluid, which causes a blockage for the main flow and a reduction of rotor capacity of 0.3% compared to the baseline. The interaction between the shroud inlet cavity and the main flow is discussed in detail in Sec. IV.C.

For the TE cutback in Fig. 10c, the flow picture changes completely at the tip end wall. The tip-passage vortex size is reduced periodically such that the indicative negative streamwise vorticity area is too small to be resolved by the measurement grid. The negative streamwise vorticity region (4) bound to the tip end wall between the blade passages is associated to the interaction of shroud exit cavity and main flow. The axial velocity component of over-tip leakage fluid is less than in the main flow due to the radial deflection at the cavity exit wall. This generates a positive tangential vorticity component, which is the dominant part of vorticity and results in a negative streamwise vorticity component. Also, the yaw angle becomes more negative in this region, creating negative axial vorticity, which adds to the negative streamwise vorticity. The comparison of region 4 in Fig. 10 shows that the designs featuring a trailing-edge cutback have a smoother radial gradient and a further penetration of negative streamwise vorticity into the main flow. For the TE cutback, the radial penetration of region 4 reaches to 85% span, 10% farther than for the baseline and the LE cutback. In addition to the changes in streamwise vorticity, the lower turbulence levels in this region, indicated by lower random fluctuations of the time-resolved pressure signal [34], suggest that the mixing of leakage and main flow is increased upstream of the measurement plane. Because the opening of the shroud exit cavity starts 78% of rotor axial chord farther upstream, the interaction of the leakage and main flow must have moved farther upstream as well for the TE cutbacks. This conclusion is also confirmed by the analysis of the radial component of the vorticity, which peaks in the velocity deficit area of the rotor wake. For the baseline, the sharp gradient between positive and negative radial vorticity from pressure to suction side of the rotor blade does not extend farther outward than 80% span due to the interaction with secondary and leakage flows. For the TE cutback, however, the wake is less disturbed for higher spanwise positions (temporarily up to the casing). The wake is therefore decoupled from the tip-passage vortex, which in turn means that the leakage fluid interacts with the tip-passage vortex at a position farther upstream, where it has not yet reached the suction side of the blade.
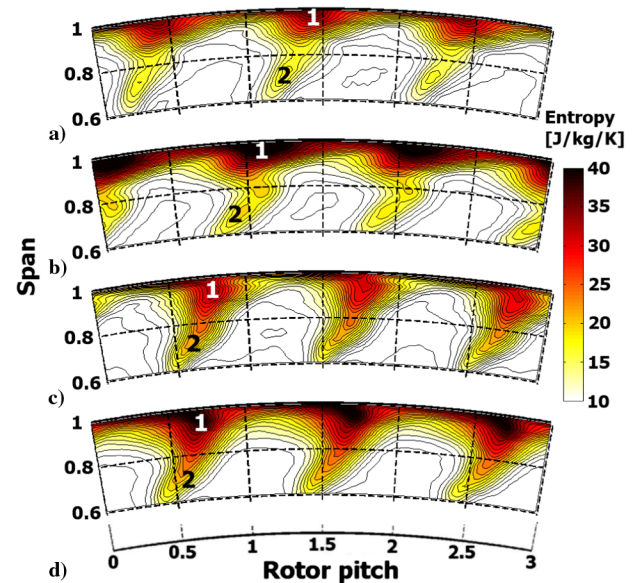
The time-averaged static entropy change relative to turbine inlet is shown at the rotor exit for all test cases in the rotor relative frame of reference in Fig. 11. Region 1 is in the same area as region 4 of Fig. 10 and therefore marks the interaction between the cavity and the main flow. The comparison of region 1 between the baseline and the LE cutback shows an increase in static entropy change of 24%. This is partly due to a change in static pressure in this location, but 80% of the increase in entropy is caused by a higher static temperature of the leakage fluid with the LE cutback. The static temperature is not only increased due to dissipation in the cavity, because the total temperature is also enhanced with the modified shroud leading edge. The heat transfer to the walls and the rotor therefore must have changed, which could be explained by a shorter residence time of the leakage fluid inside the cavity. This cannot be fully captured by the CFD calculations because the thermal boundary condition is adiabatic. The flowfield inside the cavity is discussed more in detail in Sec. IV.C.

For the TE cutback, the peak entropy change is comparable to the baseline case, but the average in the cavity interaction region is reduced. The average entropy in the wake in region 2 down to 70% span, however, is increased for both test cases featuring a shroud trailing-edge modification. This effect can be caused by two phenomena; either the profile losses in this region are increased locally, which is rather unlikely, or the high-entropy cavity fluid radially penetrates the wake on the suction of the blade. It will be shown in Sec. IV.C with the help of computational fluid dynamics that the shroud exit cavity outflow mechanism is changed for the modified shroud trailing edge and is responsible for the growth in wake thickness rather than profile losses.

The overall entropy level in the main flow is enhanced for the shroud trailing-edge modifications. This is consistent with the statement that the expansion process has changed due to the underturning of the flow for the TE cutback. On the other hand, the performance deterioration for the LE cutback is mainly due to the mass flow reduction and aerodynamic losses associated to the interaction between inlet cavity and main flow.

The time-resolved total temperature signal obtained from the FENT measurements, which is used to calculate the entropy change in Fig. 11, can also be used to track over-tip leakage fluid because there is marginal work extraction in the shroud cavity. Because the results shown in Fig. 11 are time-averaged in the relative frame of reference, all stationary components of the flow do not show here. To determine the location and moment of leakage injection from the cavity, the fully time-resolved total temperature has to be analyzed. The data show a stationary region close to the tip end wall with an

increased total temperature of more than 10 K, which is 40% of the total temperature drop across the rotor in the main flow. This region coincides with low-static-pressure regions on the suction side of the second stator. The outflow of the shroud exit cavity is therefore dominated by the stationary vanes. The matching with the low-static-pressure region caused by the potential field of the downstream vane speaks for a dominance of the second stator, especially for the baseline and the LE cutback. This means that the flowfield in the shroud exit cavity is dominated by the stators for the baseline and LE cutback. Because the vane count for both stators is identical, the influence of the inlet guide vane could only be excluded by clocking experiments or changing its vane count. The superposition of the rotor potential field at the trailing edge then modulates the outflow from the cavity and leads to a maximum outflow when the potential fields of both suction sides overlap. For the TE cutbacks, the modulation of the stationary region of high total temperature is enhanced, which means that the flowfield in the exit cavity is more rotor-dominated.

B. Multistage Performance

The one-and-a-half-stage performance of the baseline is again the highest of all test cases. Both LE cutback and TE cutback show a reduction of normalized total-to-total efficiency of 0.5%. The original design of the second stator was intended to cope with multiple operating conditions and various inlet flowfields [34]. The fact that the incidence on the leading edge of the vanes is similar in magnitude for both isolated cutbacks ($+8$ deg for LE cutback at 85% span, -7 deg for the TE cutback) and results in an identical reduction of performance proves the robust design of the second stator vanes. Because the combined cutback shows the combined effects of the two cutbacks with an emphasis on the trailing-edge modification, the total deviation from the baseline is the highest, and therefore the reduction of 0.7% in total to total efficiency is consistent with the previous observations.

Figure 12 shows that the downstream rotor will have to cope with the least incidence with the LE cutback when comparing to the baseline. In this case, the incidence on the rotor blades is less than ± 1.5 deg compared to the baseline, which would allow using the same rotor design without major drawbacks in terms of multistage efficiency. The incidence is significantly increased for the designs with a shroud trailing-edge modification.

For the TE cutback case, the incidence is within ± 4.5 deg, whereas it increases asymmetrically to up to $+8$ deg at 90% span for the combined cutback. The positive incidence at the tip increases the loading locally. This alters both the secondary flow formation as well as the interaction with the tip-shroud cavity. The in- and outflow from the cavity are expected to be intensified as the higher loading goes along with higher-pressure gradients from suction to pressure side. This will result in a growing efficiency deficit for the shroud trailing-edge modifications over multiple stages.
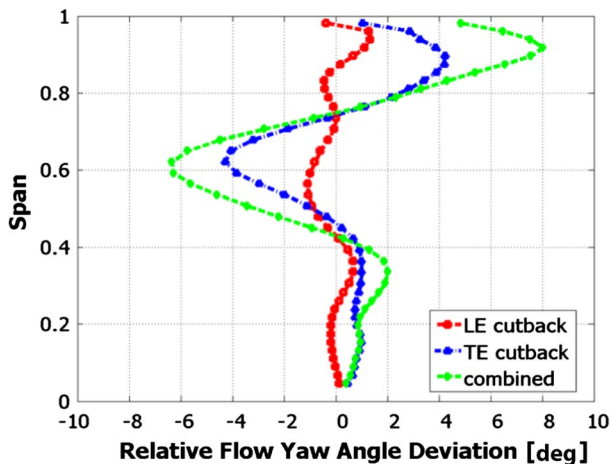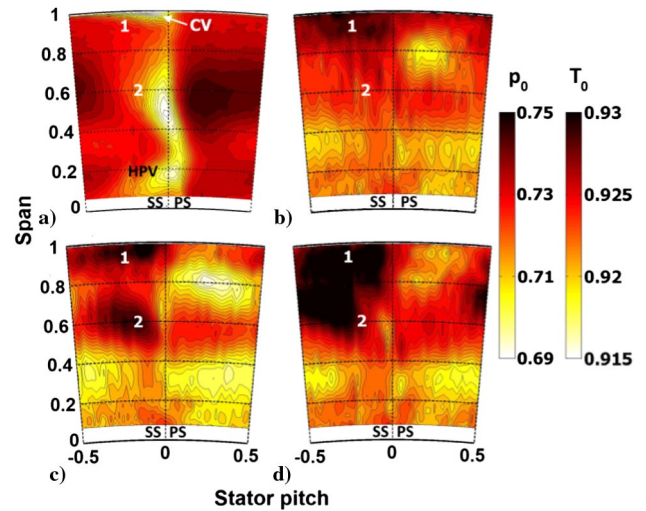
Fig. 13   Representations of time-averaged normalized a) total pressure (FRAP) at for the baseline, total temperature (FENT) for b) LE, c) TE, and d) combined cutback at stator 2 exit.

The propagation of leakage fluid and secondary flows can be traced through the second stator by analyzing the total temperature field at the exit of the second vane row. High total temperature at rotor exit is an indicator of less work extraction. At the rotor exit, the increase in total temperature at the tip due to leakage flow has already been discussed in line with the unsteady entropy change.

Figure 13a shows the normalized total pressure distribution at stator 2 exit for the baseline case. The plot is centered on the wake of the second stator, which is indicated by a distinct radial structure of low total pressure. The bulge of this zone close to the hub is associated to the stator 2 hub passage vortex. At the tip end wall, a counterclockwise corner vortex is found. In region 1 on Fig. 13b, an increase in total temperature relative to the main flow can be found. For the LE cutback, the only region with increased total temperature at rotor exit compared to the baseline has been observed in the shroud exit cavity outflow, which leads to the conclusion that the high total temperature rotor shroud leakage fluid is accumulated on the suction side of the vane between 80% span and the tip end wall. The main difference between part Figs. 13b and 13c can be found in region 2. For the TE cutback, the high total temperature fluid is partly injected into the rotor suction-side boundary layer and accumulates at 60% span on the suction side of stator 2. The rotor tip secondary flows accumulate in this area as well and explain the increased thickness of the low total pressure zone 2 around midspan in Fig. 13a. For the combined cutback in Fig. 13d, the superimposed effects of the LE cutback and the TE cutback can be observed again and lead to the highest total temperature at stator 2 exit for all test cases.

C. Over-Tip Leakage Flow

The baseline shows a rather constant pressure distribution in each of the three shroud cavities, as shown in Fig. 14. At the exit wall in the third cavity, the pressure level is increased by the radial deflection of the leakage jet from the second sealing fin. The overall pressure drop across the shroud of 12% of the turbine total inlet pressure is split equally on both fins. Hence, the discharge coefficient for both seals is identical. Numerical particle tracks show that the over-tip leakage, which is calculated to be 1.9% of the main mass flow for the baseline, passes the intermediate cavity almost directly. Only a few particles are entrained by the toroidal vortex between the two fins. The incidence of the flow on both seals is close to axial because the pumping is done by a similar toroidal vortex structure in both cavities.

For the LE cutback, the average pressure level is 1% higher in the inlet cavity. The overall pressure drop across the shroud is comparable to the baseline, but the drop across the fins is not equal. The leakage mass flow is computed to be also 1.9%, but the fluid exchange between the main flow and the shroud inlet cavity has

Fig. 12   Deviation of mass-averaged relative flow yaw angle from the baseline at stator 2 exit.
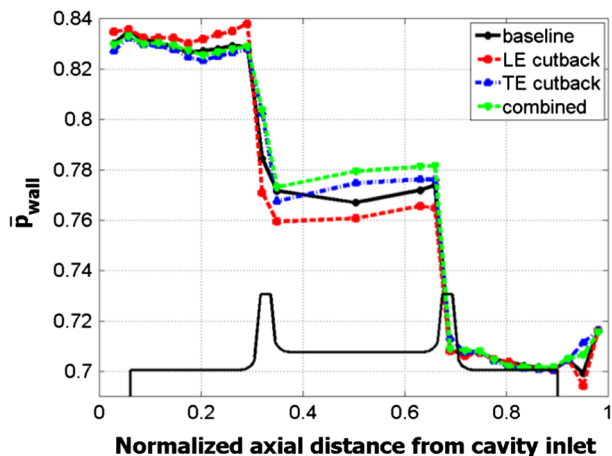
Fig. 14   Circumferentially averaged, normalized static cavity tip wall pressure.

grown from 0.3 to 2.3% of the total mass flow. Thus, for the LE cutback, the back flow is bigger than the actual leakage flow. Because the total leakage mass flow does not change, the discharge coefficient of the seals must change for the LE cutback. As a conclusion, the pressure overhead in front of the first fin has to be caused by a radial velocity component of the incoming flow.

The TE cutback generally follows the trend of the baseline curve, except in the intermediate cavity and directly in front of the exit wall. This leads to the conclusion that the inlet cavity and the leakage flow across the shroud are not affected by the trailing-edge cutback because the overall predicted leakage mass flow is also 1.9% for this case. The modification of the shroud trailing edge does not reach out to the outer casing in terms of pressure, where the pressure tappings are installed.

For the combined cutback, the effects of the shroud leading-edge modification are not captured by the tappings at the wall. The inlet cavity pressure level is close to the baseline, suggesting that the radial flows found for the LE cutback disappeared and that the two different leading-edge modifications do not have a scalable effect on the cavity flowfield.

Figure 15 shows the time-averaged static wall pressure in the inlet cavity in the rotating frame of reference for the baseline (Fig. 15a) and the two designs featuring a shroud leading-edge modification. For the baseline, the stagnation point of the cavity inflow is marked by a high static pressure at around 10% axial distance from the inlet wall. The presence of this high pressure level on the whole pitch suggests that the influence of the upstream vane is dominant and only modulated by the rotor passing. The peak pressure is then found above the pressure side of the rotor leading edge when the two potential fields of stator vane and rotor blade add up. Predicted particle tracks show that two toroidal vortices are created upstream and downstream of this stagnation point. The fluid that is deflected toward the inlet wall forms a radially stretched toroidal vortex with positive tangential vorticity. This part of the cavity flow is reinjected into the main flow when the rotor and stator suction-side potential field are superimposed. The major part (85%) of the cavity fluid, however,
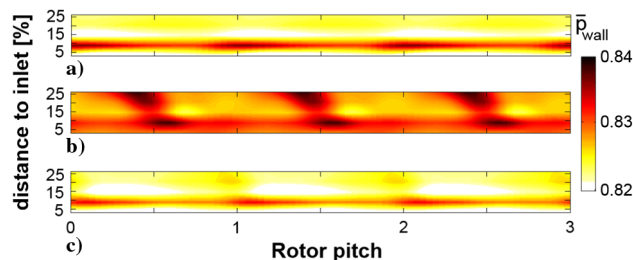
is accelerated toward the sealing fin and forms a rather symmetric toroidal vortex with negative tangential vorticity. Before crossing the seal, the main part of the cavity inflow is entrained by this toroidal vortex. This behavior depends on the cavity geometry and has been observed in several other studies (e.g., [17,18]).

Contrary to the baseline, the flowfield of the LE cutback in Fig. 15b is dominated by the rotor. The stagnation line observed for the baseline is still present, with a higher peak pressure in front of the rotor leading edge. Additionally, there are rotor-locked high-pressure zones, which extend axially to the first sealing fin. Although the spatial resolution of the pressure transducers is limited, the shape of the shroud leading-edge platform can be recognized in the pressure field. This indicates that permanent radial jets are pumped into the cavity. The combined cutback pressure field shown in Fig. 15c resembles very much the one of the baseline. In front of the sealing fin, only a slight increase is shown per rotor passage, indicating that the jets of the LE cutback are no longer present.

The predicted particle tracks in Fig. 16a as well as the radial velocity distribution at the interface with the main flow shown in Fig. 17a confirm this result. The two toroidal vortex systems found for the unmodified cavity are completely suppressed by the shroud leading-edge modification in the LE cutback case. Instead, a highly three-dimensional flowfield is found attached to each leading edge of the rotor. Depending on the relative position to the shroud, the inflow splits into several vortical structures, out of which three are described more in detail here. Figure 16b shows tracks of fluid, which enters the cavity close to the sealing fin. This portion of fluid passes the seal after a deflection of close to 90 deg directly. The extreme curvature of these streamlines leads to a higher blockage in front of the first seal and explains the increased pressure drop across the first seal for the LE cutback.

The part of the flow that enters farther upstream and very close to the shroud as shown in Fig. 16c is entrained in a vortex with negative tangential vorticity forming on top of the shroud platform. The
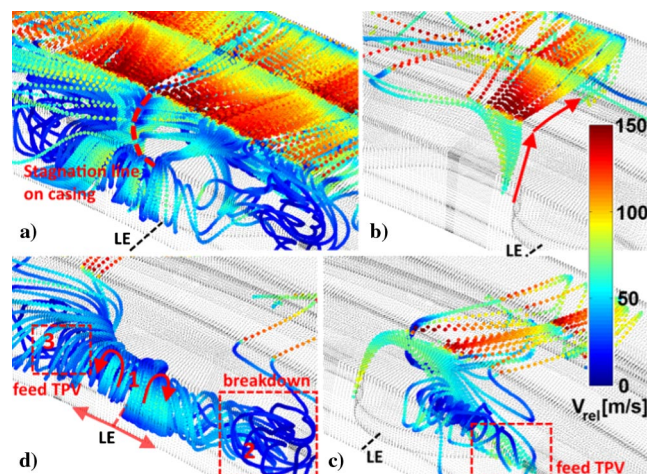
Fig. 16   Predicted trajectories into the LE cutback cavity of a) all particles, particles entering b) close to seal, c) on the blade pressure side, and d) upstream of the blade LE.

Fig. 15   Measured time-averaged, normalized static wall pressure in the rotating frame of reference in the shroud inlet cavity: a) baseline, b) LE, and c) combined cutback.
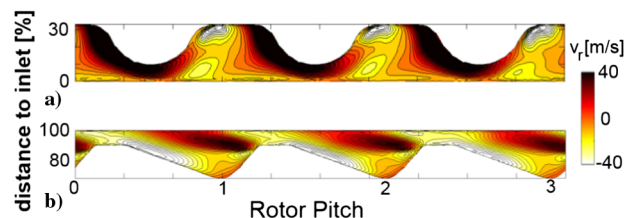
Fig. 17   Simulated radial velocity at the interface to the main flow for a) the LE cutback at the inlet cavity and b) the TE cutback at the exit cavity.

development of a toroidal vortex system is suppressed by the increased mass flow entering the cavity close to the leading edge of the blade in Fig. 16d. The movement of the incoming fluid is constrained by the vortical structures on top of the shroud platform and is forced to roll up into a vortex with positive tangential vorticity. At location 1, this structure splits into two parts moving toward the adjacent flow passages between the rotor blades. The part of the vortex following the rotation of the rotor breaks down when it touches its equivalent from the next blade in region 2. The part of the structure moving around the pressure side of the leading edge is fed by the incoming fluid on the pressure side of the leading edge farther away from the shroud than in Fig. 16c and therefore does not break down but is blocked and deflected in axial direction. The positive tangential vorticity is transformed into negative axial vorticity by this process in region 3. When this turned flow structure reenters the main flow closer to the suction side of the adjacent blade, indicated by the negative radial velocity in Fig. 17a, the sense of rotation matches the pressure-side leg of the horseshoe vortex and therefore leads to an intensification of the passage vortex. The maximum radial velocities are similar for the baseline and the LE cutback (60 m/s); however, the total inflow increased by approximately a factor of 2 (4.2% of total mass flow) due to the larger inflow area. All predicted paths of particles reentering the main flow merge the tip-passage vortex. This contributes to its increase in size and strength observed at the rotor exit as well as the associated reduction in rotor capacity.

Figure 18 shows the equivalent pressure distribution for the shroud exit cavity of the baseline (Fig. 18a) and the two designs with a shroud trailing-edge modification. The baseline again shows a circumferential distribution of static pressure associated to the influence of a stationary vane. At 80% axial cavity length, a rotor-locked increase in static pressure can be observed. This is either related to the leakage jets or the toroidal vortex in the exit cavity. The pneumatic tappings are not capable of capturing this pressure rise. The particle tracking calculations predict that the majority of the leakage jet behind the second fin is deflected inward and directly enters the main flow. The smaller part of the deflected leakage jet enters the toroidal vortex with negative tangential vorticity on the shroud trailing-edge platform.

For the TE cutback in Fig. 18b, an amplification of the pressure rise of the baseline is detected. This is related to the fact that the leakage jet does not leave the cavity directly as in the baseline case but is first entrained into the toroidal vortex of the exit cavity. The picture for the
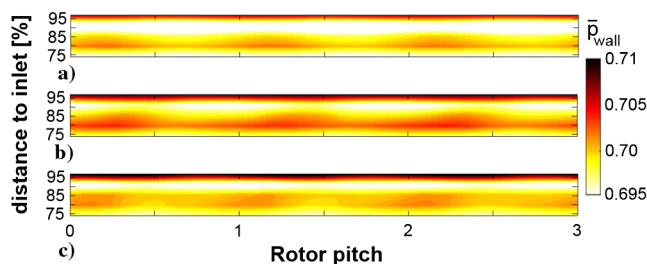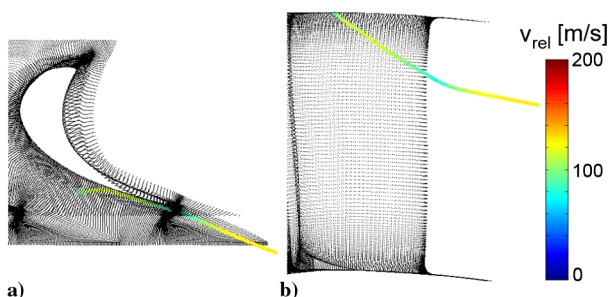
combined cutback in Fig. 18c is similar but more scrambled during the phase-locking due to higher unsteadiness.

Figure 17b shows the radial velocity distribution for the TE cutback in the rotor-relative frame at the interface to the main flow. The integration shows that the total amount of over-tip leakage remains constant at 1.9% of the main mass flow, but the additional inflow into the shroud exit cavity is 2% of the main mass flow (i.e., doubled compared to the baseline). Again, the cutback enforces the flow to enter the cavity on the pressure side of the rotor blades directly behind the throat. This flow blocks the over-tip leakage jet and is accelerated in circumferential direction by the contraction between the exit cavity wall and the suction-side part of the shroud trailing edge. Depending on the injection position, the intruding fluid is entrained by a toroidal vortex above the shroud platform or deflected toward the suction side, which creates a locally reversed flow. On the suction side, it is injected at 20% (axially, 75% streamwise) of the axial blade chord farther upstream into the boundary layer of the airfoil. Figure 19 shows a typical particle track for the described flow path. The cavity outflow penetrates the suction side farther than 70% span, which is consistent with the measurement results on the rotor exit plane. The locally increased levels of entropy around the rotor wake area shown in Figs. 11c and 11d are also found in the relative total pressure data. The distance of the isolines on the pressure and suction side indicate that the rotor wake grows by a factor of 1.5–2 in the pitchwise direction for the TE cutback and goes along with a reduction of the relative Mach number where the cavity fluid is injected into the boundary layer. The flow leaving the shroud exit cavity at a greater cross streamwise distance from the suction side of the blade crosses the path of the tip-passage vortex. The passage vortex is therefore prevented from entraining more low-momentum fluid from the shroud end wall and the blade suction side, which explains its weakening and temporal extinction.

V. Conclusions

This paper provides detailed insight into the fluid dynamics of three different partial shroud designs and helps the designer choosing a shroud design according to the optimization goals. Clearly, the aerodynamic performance of a fully shrouded turbine rotor is superior to partially shrouded turbines. The weight reduction associated to each cutback design scales with the tip blade pitch and is limited by the sealing fin positions, which can point out the feasibility of shrouded versus unshrouded blades very early in the design phase.

Independent of the location, the reduction of the shroud platform area has two consequences. First, the fluid exchange between the main flow and the shroud cavities is increased. In the present study, the mass flow exchange is estimated to double for the partial shrouds. However, the mean over-tip leakage mass flow remains constant. Second, the vortical structures controlling the fluid pumping in the cavities are significantly affected. For the LE cutback case, this leads to a direct feeding of the tip-passage vortex and hence a blockage within the rotor. In this case, the efficiency drops by 0.7% compared to the baseline. Although the cavity flowfield appears to be beneficial in terms of losses for the TE cutback, the reinjection of cavity fluid into the boundary layer of the blade suction side leads to an underturning of the flow. The reduction of angular momentum exchange leads to the same efficiency penalty as for the LE cutback.

The combined cutback has an equivalent material removal from the shroud as for the LE cutback. It superimposes the fluid dynamic effects observed for the isolated cutbacks and adds the losses up to an efficiency reduction of 1.1% compared to the baseline. Although the incidence variation on the downstream stator is the highest for the LE cutback, the multistage performance and the incidence on the rotor of the next stage are favorable for this type of shroud modification. The accumulation of fluid with increased total temperature on the suction side of the downstream vane might lead to local hot spots in real gas turbines and counteracts the mass reduction achieved with partial shrouds.

Altogether, the LE cutback yields the highest shroud mass reduction with the lowest aerodynamic efficiency penalty. The combination of these effects leads to the conclusion that, when the

Fig. 18 Measured time-averaged, normalized static wall pressure in the rotating frame of reference in the shroud exit cavity: a) baseline, b) TE cutback, and c) combined cutback.

Fig. 19 Flow path of a particle leaving the shroud exit cavity of the TE cutback: a) top view and b) view onto the suction side.

need for blade stress reduction outweighs aerodynamic performance criteria, material should only be removed from the shroud leading edge.

Acknowledgments

References

[1] Wu, X., Vahdati, M., Schipani, C., and Imregun, M., "Analysis of Low-Pressure Turbine Flutter for Different Shroud Interfaces," *Proceedings of the ASME Turbo Expo*, American Soc. of Mechanical Engineers Paper GT2007-27377, 2007.

[2] Kurzke, J., "Fundamental Differences Between Conventional and Geared Turbofans," *Proceedings of the ASME Turbo Expo*, American Soc. of Mechanical Engineers Paper GT2009-59745, 2009.

[3] Lyon, T. A., and Hillery, R. D., "Geared Fan Engine Systems—Their Advantages and Potential Reliability," *Journal of Aircraft*, Vol. 10, No. 6, 1973, pp. 361–365.
doi:10.2514/3.60237

[4] Camci, C., Dey, D., and Kavurmacioglu, L., "Aerodynamics of Tip Leakage Flows near Partial Squealer Rims in an Axial Flow Turbine Stage," *Journal of Turbomachinery*, Vol. 127, No. 1, 2005, pp. 14–24.
doi:10.1115/1.1791279

[5] Selic, T., Lengani, D., Marn, A., and Heitmeir, F., "Aerodynamic Effects of an Unshrouded Low Pressure Turbine on a Low Aspect Ratio Exit Guide Vane," *Proceedings of the ASME Turbo Expo*, American Soc. of Mechanical Engineers Paper GT2012-68981, 2012.

[6] Harvey, N. W., "Aerothermal Implications of Shroudless and Shrouded Blades," *Turbine Blade Tip Design and Tip Clearance Treatment*, von Karman Inst. Lecture Series, von Karman Inst. for Fluid Dynamics, Sint-Genesius-Rode, Belgium, 2004, pp. 1–120; also VKI LS 2004-02, "Turbine Blade Tip Design and Tip Clearance Treatment," 2004, pp. 1–120.

[7] Kaiser, I., and Bindon, J. P., "The Effect of Tip Clearance on the Development of Loss Behind a Rotor and a Subsequent Nozzle," American Soc. of Mechanical Engineers Paper 97-GT-053, 1997.

[8] Mischo, B., Behr, T., and Abhari, R. S., "Flow Physics and Profiling of Recessed Blade Tips: Impact on Performance and Heat Load," *Journal of Turbomachinery*, Vol. 130, No. 2, 2008, pp. 1–8.
doi:10.1115/1.2775485

[9] Harvey, N. W., and Ramsden, K., "A Computational Study of a Novel Turbine Rotor Partial Shroud," *Journal of Turbomachinery*, Vol. 123, No. 3, 2001, pp. 534–543.
doi:10.1115/1.1370166

[10] Dey, D., and Camci, C., "Aerodynamic Tip De-Sensitization of an Axial Turbine Rotor Using Tip Platform Extensions," American Soc. of Mechanical Engineers Paper 2001-GT-484, 2001.

[11] Zhou, C., Hodson, H., Tibbott, I., and Stokes, M., "Effects of Winglet Geometry on the Aerodynamic Performance of Tip Leakage Flow in a Turbine Cascade," *Journal of Turbomachinery*, Vol. 135, No. 5, 2013, Paper 051009.
doi:10.1115/1.4007831

[12] Denton, J. D., "Loss Mechanisms in Turbomachines," *Journal of Turbomachinery*, Vol. 115, No. 4, 1993, pp. 621–656.
doi:10.1115/1.2929299

[13] Wallis, A. M., Denton, J. D., and Demargne, A. A. J., "The Control of Shroud Leakage Flows to Reduce Aerodynamic Losses in a Low Aspect Ratio Shrouded Axial Flow Turbine," *Journal of Turbomachinery*, Vol. 123, No. 2, 2001, pp. 334–341.
doi:10.1115/1.1354143

[14] Rosic, B., and Denton, J. D., "Control of Shroud Leakage Loss by Reducing Circumferential Mixing," *Journal of Turbomachinery*, Vol. 130, April 2008, pp. 1–7.

[15] Anker, J. E., Mayer, J. F., and Casey, M. V., "The Impact of Rotor Labyrinth Seal Leakage Flow on the Loss Generation in an Axial Turbine," *Proceedings of the Institution of Mechanical Engineers, Part A: Journal of Power and Energy*, Vol. 219, Sept. 2005, pp. 483–490.

[16] Pfau, A., Kalfas, A. I., and Abhari, R. S., "Making Use of Labyrinth Interaction Flow," *Transactions of the ASME*, Vol. 129, Jan. 2007, pp. 164–174.

[17] Barmpalias, K. G., Abhari, R. S., Kalfas, A. I., Hirano, T., Shibukawa, N., and Sasaki, T., "Design Considerations for Axial Steam Turbine Rotor Inlet Cavity Volume and Length Scale," *Journal of Turbomachinery*, Vol. 134, No. 5, 2012, Paper 051031.
doi:10.1115/1.4004827

[18] Giboni, A., Menter, J. R., Peters, P., Wolter, K., Pfost, H., and Breisig, V., "Interaction of Labyrinth Seal Leakage Flow and Main Flow in an Axial Turbine," *Proceedings of the ASME Turbo Expo*, American Soc. of Mechanical Engineers Paper GT2003-38722, 2003.

[19] Rosic, B., Denton, J. D., and Curtis, E. M., "The Influence of Shroud and Cavity Geometry on Turbine Performance: An Experimental and Computational Study—Part 1: Shroud Geometry," *Journal of Turbomachinery*, Vol. 130, No. 4, 2008, pp. 1–10.

[20] Barmpalias, K. G., Kalfas, A. I., Chokani, N., and Abhari, R. S., "The Dynamics of the Vorticity Field in a Low Solidity Axial Turbine," *Proceedings of the ASME Turbo Expo*, American Soc. of Mechanical Engineers Paper GT2008-51142, 2008.

[21] Gier, J., Stubert, B., Brouillet, B., and de Vito, L., "Interaction of Shroud Leakage Flow and Main Flow in a Three-Stage LP Turbine," *Journal of Turbomachinery*, Vol. 127, No. 4, 2005, pp. 649–658.
doi:10.1115/1.2006667

[22] Nirmalan, N. V., and Bailey, J. C., "Experimental Investigation of Aerodynamic Losses of Different Shapes of a Shrouded Blade Tip Section," *Proceedings of the ASME Turbo Expo*, American Soc. of Mechanical Engineers Paper GT2005-68903, 2005.

[23] Porreca, L., Behr, T., Schlienger, J., Kalfas, A. I., Abhari, R. S., Ehrhard, J., and Janke, E., "Fluid Dynamics and Performance of Partially and Fully Shrouded Axial Turbines," *Journal of Turbomachinery*, Vol. 127, No. 4, 2005, pp. 668–678.
doi:10.1115/1.2008972

[24] Porreca, L., Kalfas, A. I., and Abhari, R. S., "Optimized Shroud Design for Axial Turbine Aerodynamic Performance," *Journal of Turbomachinery*, Vol. 130, No. 3, 2008, pp. 1–12.
doi:10.1115/1.2777187

[25] Feldman, G. M., Strasser, W. S., Wilkins, F. C., and Leylek, J. H., "Transonic Passage Turbine Blade Tip Clearance with Scalloped Shroud: Part 1—Aerodynamics Losses in a Dual-Passage Cascade," *IMECE04*, American Soc. of Mechanical Engineers Paper IMECE2004-59115, 2004.

[26] Behr, T., Kalfas, A. I., and Abhari, R. S., "Unsteady Flow Physics and Performance of a One-and-1/2-Stage Unshrouded High Work Turbine," *Journal of Turbomachinery*, Vol. 129, No. 2, 2008, pp. 348–359.
doi:10.1115/1.2447707

[27] Schuepbach, P., Abhari, R. S., Rose, M. G., and Gier, J., "Sensitivity of Turbine Efficiency and Flow Structures to Varying Purge Flow," *Journal of Propulsion and Power*, Vol. 26, No. 1, 2010, pp. 46–56.
doi:10.2514/1.44646

[28] Jenny, P., Abhari, R. S., Rose, M. G., Brettschneider, M., and Gier, J., "A Low Pressure Turbine with Profiled End Walls and Purge Flow Operating with a Pressure Side Bubble," *Journal of Turbomachinery*, Vol. 134, No. 6, 2012, pp. 1–9.
doi:10.1115/1.4006303

[29] Kupferschmied, P., Kopperl, O., Gizzi, W. P., and Gyarmathy, G., "Time Resolved Flow Measurements with Fast Aerodynamic Probes in Turbomachinery," *Journal of Measurement Science and Technology*, Vol. 11, No. 7, 2000, pp. 1036–1054.
doi:10.1088/0957-0233/11/7/318

[30] Pfau, A., Schlienger, J., Kalfas, A. I., and Abhari, R. S., "Unsteady, 3-Dimensional Flow Measurement Using a Miniature Virtual 4-Sensor Fast Response Aerodynamic Probe (FRAP)," *Proceedings of the ASME Turbo Expo*, American Soc. of Mechanical Engineers Paper GT2003-38128, 2003.

[31] Mansour, M., Chokani, N., Kalfas, A. I., and Abhari, R. S., "Time-Resolved Entropy Measurements Using a Fast Response Entropy Probe," *Measurement Science and Technology*, Vol. 19, Sept. 2008, pp. 1–14.

[32] Behr, T., "Control of Rotor Tip Leakage and Secondary Flow by Casing Air Injection in Unshrouded Axial Turbines," Ph.D. Dissertation, Swiss Federal Inst. of Technology, Zurich, 2007.

[33] Mansour, M., Chokani, N., Kalfas, A. I., and Abhari, R. S., "Impact of Time-Resolved Entropy Measurement on a One-and-One-Half-Stage Axial Turbine Performance," *Journal of Turbomachinery*, Vol. 134, No. 2, 2012, Paper 021008.
doi:10.1115/1.4003247

[34] Porreca, L., Kalfas, A. I., Abhari, R. S., and Hollenstein, M., "Turbulence Measurements and Analysis in a Multistage Axial Turbine," *Journal of Power and Propulsion*, Vol. 23, No. 1, 2007, pp. 227–234.
doi:10.2514/1.20022

T. J. Praisner
Associate Editor